



Article

Expected Precision of Gravity Gradient Recovered from Ka-Band Radar Interferometer Observations and Impact of Instrument Errors

Hengyang Guo ^{1,2} , Xiaoyun Wan ^{1,2,*}, Fei Wang ¹ and Song Tian ¹

¹ School of Land Science and Technology, China University of Geosciences (Beijing), Beijing 100083, China; ghy2022@email.cugb.edu.cn (H.G.); 2012200015@cugb.edu.cn (F.W.); tiansong-heny@powerchina.cn (S.T.)

² Key Laboratory of Smart Earth, Beijing 100029, China

* Correspondence: wanxy@cugb.edu.cn

Abstract: Full tensor of gravity gradients contains extremely large amounts of information, which is one of the most important sources for research on recovery seafloor topography and underwater matching navigation. The calculation and accuracy of the full tensor of gravity gradients are worth studying. The Ka-band interferometric radar altimeter (KaRIn) of surface water and ocean topography (SWOT) mission enables high spatial resolution of sea surface height (SSH), which would be beneficial for the calculation of gravity gradients. However, there are no clear accuracy results for the gravity gradients (the gravity gradient tensor represents the second-order derivative of the gravity potential) recovered based on SWOT data. This study evaluated the possible precision of gravity gradients using the discretization method based on simulated SWOT wide-swath data and investigated the impact of instrument errors. The data are simulated based on the sea level anomaly data provided by the European Space Agency. The instrument errors are simulated based on the power spectrum data provided in the SWOT error budget document. Firstly, the full tensor of gravity gradients (SWOT_GGT) is calculated based on deflections of the vertical and gravity anomaly. The distinctions of instrument errors on the ascending and descending orbits are also taken into account in the calculation. The precision of the T_{zz} component is evaluated by the vertical gravity gradient model provided by the Scripps Institution of Oceanography. All components of SWOT_GGT are validated by the gravity gradients model, which is calculated by the open-source software GrafLab based on spherical harmonic. The T_{zz} component has the poorest precision among all the components. The reason for the worst accuracy of the T_{zz} component may be that it is derived by T_{xx} and T_{yy} , T_{zz} would have a larger error than T_{xx} and T_{yy} . The precision of all components is better than 6 E. Among the various errors, the effect of phase error and KaRIn error (random error caused by interferometric radar) on the results is greater than 2 E. The effect of the other four errors on the results is about 0.5 E. Utilizing multi-cycle data for the full tensor of gravity gradients recovery can suppress the effect of errors.

Keywords: surface water and ocean topography (SWOT) mission; full tensor of gravity gradients; radar interferometry; satellite altimetry; marine gravity field



Citation: Guo, H.; Wan, X.; Wang, F.; Tian, S. Expected Precision of Gravity Gradient Recovered from Ka-Band Radar Interferometer Observations and Impact of Instrument Errors. *Remote Sens.* **2024**, *16*, 576. <https://doi.org/10.3390/rs16030576>

Academic Editor: Chung-yen Kuo

Received: 9 December 2023

Revised: 26 January 2024

Accepted: 31 January 2024

Published: 2 February 2024



Copyright: © 2024 by the authors. Licensee MDPI, Basel, Switzerland. This article is an open access article distributed under the terms and conditions of the Creative Commons Attribution (CC BY) license (<https://creativecommons.org/licenses/by/4.0/>).

1. Introduction

With years of development of altimetry technology [1–3], satellite altimetry data have become the primary source for inverting ocean gravity fields due to their advantages, such as shorter data acquisition cycles and wider measuring ranges compared to shipborne gravity [4–7]. It is feasible to obtain high-precision and high-resolution models of deflections of the vertical (DOV) and gravity anomalies (GA) based on altimetry data [8–11]. These models provide vital information for the study of gravity gradients. However, there is little research on gravity gradients; even the Scripps Institution of Oceanography (SIO) is only calculating the vertical gravity gradients (VGG) model. Gravity gradients reflect

the dynamic variations in GA, which is a powerful tool for detecting irregular density distributions in plates, revealing tectonic activity in the field [12]. Therefore, not only the VGG deserves attention, but also full tensor of gravity gradients with more information. The availability of gravity gradients in marine regions constitutes a foundational resource for numerous applications, such as the inversion of bathymetry, underwater matching navigation, and geological exploration, attracting increased attention [13–16].

The surface water and ocean topography (SWOT) satellite was developed jointly by National Aeronautics and Space Administration (NASA) and Centre National D'Etudes Spatiales (CNES), with contributions from many other agencies. SWOT was successfully launched on 16 December 2022. The mission aims to precisely measure global terrestrial water height and sea surface height (SSH). The development, launch, and operation of the SWOT satellite have obtained more attention from many international oceanographers [17–19], making it an important development in oceanographic research. The SWOT satellite measures the ocean surface topography with great accuracy, using interferometry to achieve two-dimensional mapping [10,20,21]. The look angles at the altitude of SWOT entail swath coverage of about 120 km (from 10 to 70 km in the cross-track distance on both sides of the nadir track). SWOT has a large potential in deriving gravity gradients due to its high spatial resolution and accuracy; the low-rate measurement model of Ka-band radar interferometer (KaRIn) has a spatial resolution of about 2 km, and spatial averaging of 1 km² improves the altimetry accuracy to less than 2 cm (<https://www.aviso.altimetry.fr/en/missions/current-missions/swot/instruments/karin-wide-swath-altimeter-in-ka-band.html>, accessed on 15 November 2023).

Jin et al. [10] simulated various instrument errors using power spectral density (PSD) data provided by Esteban-Fernandez et al. [22]. In the South China Sea and part of the Indian Ocean, significant improvements are observed in the accuracy of the east–west component of the DOV determined by one-cycle SWOT data. Yu et al. [20] proved that the inverse Vening Meinesz (IVM) exhibits more robustness in handling both random and systematic errors within the SWOT dataset compared to the inverse Stokes' integral (ISM). Additionally, multi-cycle data of SWOT can provide higher-quality GA. Ma et al. [23] performed crossover calibration between descending orbits and ascending orbits within one cycle followed by collinear adjustment across multiple cycles. This strategy resulted in an approximately 45% improvement in the accuracy of GA compared to one cycle. Liu et al. [24] systematically investigated the impact of various grid spacing and multiple directions of geoid gradients on the estimation of residual DOV (rDOV) based on simulated data. They found that instrument errors have a significant effect on rDOV. The IceSat-2 has similar characteristics to SWOT; that is they can provide SSH across-track. Liu et al. [25] derived 2' grid DOV and GA from cross-beam synchronous observations in the South China Sea based on SSH of IceSat-2, which supports the application of SWOT data.

Yu and Hwang [26] derived the VGG based on altimetry data from the Cryosat-2 and Jason-1/2. Zhou et al. [27] developed a vertical gravity anomaly gradient model with a resolution of 1' × 1' for the Arabian Sea and its surrounding regions from the altimetry data of Cryosat-2. The root mean square (RMS) compared to the VGG model provided by SIO is 7.69 E (1E = 1 × 10⁻⁹/s²). Wan et al. [28] investigated the impact of environment errors based on Tian's method [29] on the recovery of DOV and GA from wide-swath altimetry data.

Despite rapid advancements in gravity gradiometer technology [30], the measurement of marine gravity gradients using gravity gradiometers is constrained due to the limitations of space, vehicles, and cost [31]. The computation of gravity gradients remains a challenging geodetic task, particularly in marine regions.

Many studies have shown that the use of gravity gradients enhances the reliability of inversion of bathymetry and underwater gravity matching navigation [32–35]. However, most researchers primarily focus on computing VGG [26] using the derivation formula provided by Heiskanen and Moritz [36,37]. Wan et al. [15] found that few methods have been proposed to invert full tensor of gravity gradients from altimetry data. Therefore,

they proposed a fast Fourier transform (FFT) algorithm to derive the full tensor of gravity gradients using satellite altimetry data [15]. Tian [29] proposed a discretization method to compute the full tensor of gravity gradients. This method is suitable for two-dimensional altimetry data and effectively utilizes data from neighboring grid points, avoiding extensive integration calculations.

The expected precision of the derived full tensor of gravity gradients based on SWOT data (SWOT_GGT) is not clear. In this study, the method of Tian [29] is used to derive the SWOT_GGT and give the expected precision of the results. According to the latest updates, the SWOT team is calibrating the data with the latest technology and we are looking forward to the release of “Pre-Validated” science data. Before the release of “Pre-Validated” data, we still need to perform some experiments based on the simulated data, because the simulated data can control variables in studying the impact of the instrument errors on SWOT_GGT. In Section 2, the research area and data are introduced. Section 3 presents the discretization method to compute SWOT_GGT. In Section 4, the SWOT_GGT is established, and the accuracy of SWOT_GGT is evaluated. In addition, the impact of instrument errors on the calculation of full tensor of gravity gradients is also analyzed. Section 5 discusses the effect of instrument errors when calculating SWOT_GGT using multi-cycle data. Finally, Section 6 provides the conclusion.

2. Study Area and Data

2.1. Study Area

The study is conducted over the Bay of Bengal and its surrounding areas (BOB), located in the northern Indian Ocean (80°E – 100°E , 0°N – 23°N). The area encompasses the global largest turbidite alluvial fan system and basins, resulting in complex seafloor topography [38]. The location of the area and its seafloor topography is shown in Figure 1. The seafloor topography of the study area (as shown in Figure 1) corresponds to the DTU21 bathymetric model, which is one of the most accurate models for seafloor topography [35].

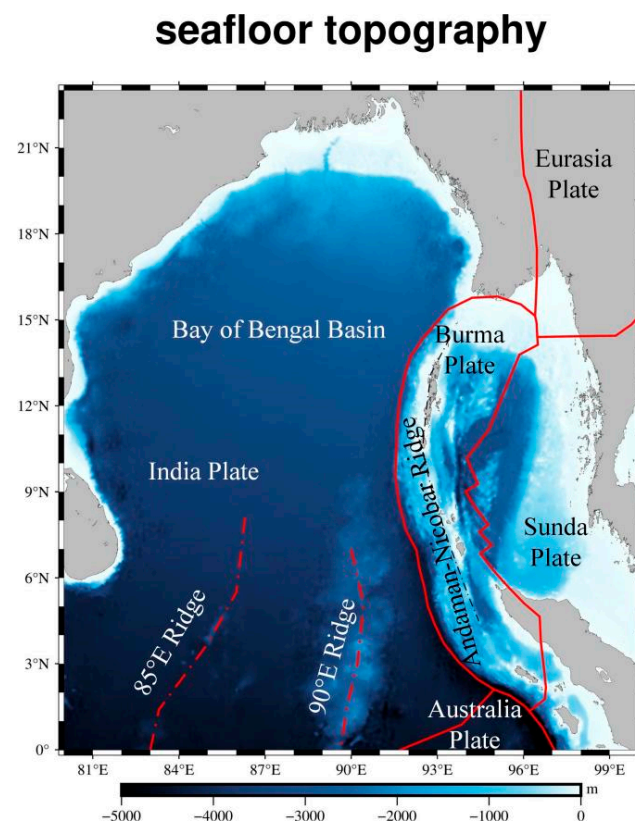


Figure 1. The Bay of Bengal and its surrounding areas. The red solid line represents the boundary between tectonic plates, while the red dashed line indicates the approximate location of Ridges.

As a result of the movements of the Indian Plate and the Burma Plate, the area has undergone significant sedimentation, leading to a remarkably diverse topography. Notable features include the 90°E Ridge, the Andaman–Nicobar Ridge, and the Bay of Bengal Basin [39]. Consequently, this region provides favorable conditions for conducting scientific research aimed at obtaining high-precision marine gravity field products.

2.2. Data

The datasets adopted in this study are listed in Table 1.

Table 1. The information on the datasets used in this paper.

Datasets	Resolution	Provider
Sea level anomaly (SLA)	15'	European Space Agency (ESA)
Mean sea surface (MSS) MSS_CNES_CLS2015	1'	CNES
Mean dynamic topography (MDT) MDT_CNES_CLS18	7.5'	CNES
DTU21 bathymetric model	1'	Technical University of Denmark (DTU)
XGM2019e	1'	Technical University of Munich (TUM)
EGM2008	1'	National Geospatial-Intelligence Agency (NGA)
SIO V32.1 datasets	1'	SIO
Shipborne gravity data	Distributed along the survey trajectory	National Centers for Environmental Information (NCEI)
GrafLab_GGT	1'	Calculated by GrafLab-1.1.2 utilizes spherical harmonics based on the EGM2008 gravity field model

Since the experiments are conducted based on simulated science orbit (21-day) data, it is necessary to simulate SSH data. The tool used for simulating is the `swot_simulator-1.2.4` provided by JPL (https://github.com/CNES/swot_simulator, accessed on 15 November 2023). Utilizing input SLA data provided by ESA [40], the format of data is transformed to wide-swath. Instrument errors are introduced into the wide-swath data. The instrument errors are simulated based on PSD data provided by JPL [22]. After this step, we obtain SLA data with all simulated instrument errors. Then, by adding the mean sea surface height (MSS_CNES_CLS2015) [41], we obtain the SSH data used for the experiments, i.e., $SSH = SLA + MSS$. By subtracting the mean dynamic topography (MDT_CNES_CLS18) [42], the topography of the sea surface is removed, allowing for the determination of geoid heights at the grid points, i.e., $Geoid = SSH - MDT$. Geoid data can be used to calculate rDOV; the formulas are shown in Appendix A.

The SSH data are filtered by the one-dimensional Gauss filter to deal with the influence of sea level variations and noise. The STD of the width of the filter is set to 10 km. This filtering process may result in the loss of a part of short-wavelength data [20], but the limitations caused by the absence of the shortest wavelengths are relatively minimal.

In addition to the data used for simulating SWOT data mentioned above, other datasets are employed for experiments and validating the results. Among them, the XGM2019e model [43] is used as the reference gravity field model in the remove–restore procedure. The SIO V32.1 datasets include `east_32.1`, `north_32.1`, `grav_32.1`, and `curv_32.1`. These models are considered to be some of the most accurate global high-resolution and high-precision gridded models for ocean gravity [44].

The shipborne gravity dataset comprises a collection of measured marine gravity data from various departments using different instruments [45]. Before using the ship-

borne gravity data, they needs to be adjusted by removing gross errors using a quadratic polynomial in time [46].

GrafLab_GGT is utilized to validate all components of SWOT_GGT. GrafLab_GGT is generated by GrafLab based on the EGM2008 model expanded to degree and order 2159 [47] (since XGM2019e is used as the reference gravity field when calculating DOV and GA, the EGM2008 is used to calculate the GrafLab_GGT during the validation to avoid correlation). The GrafLab-1.1.2 is an open-source software, which can compute various functionals of the geopotential up to ultra-high degrees using spherical harmonic expansion based on the gravity field model [48].

2.3. SWOT Wide-Swath Data and Simulated Errors

Six types of errors are simulated according to the PSDs defined in SWOT error budget file, including random error caused by KaRIn (KaRIn error), roll error (caused by the gyro error and roll control error), phase error (caused by the interferometer technology), baseline dilation error (caused by the baseline of KaRIn), timing error (errors in the time-tagging accuracy of the payload data), and wet troposphere error (caused by the humid atmosphere) [22,49]; all these errors directly affect the SSH data. Figure 2 shows the spatial distribution of individual errors and the total error in one cycle.

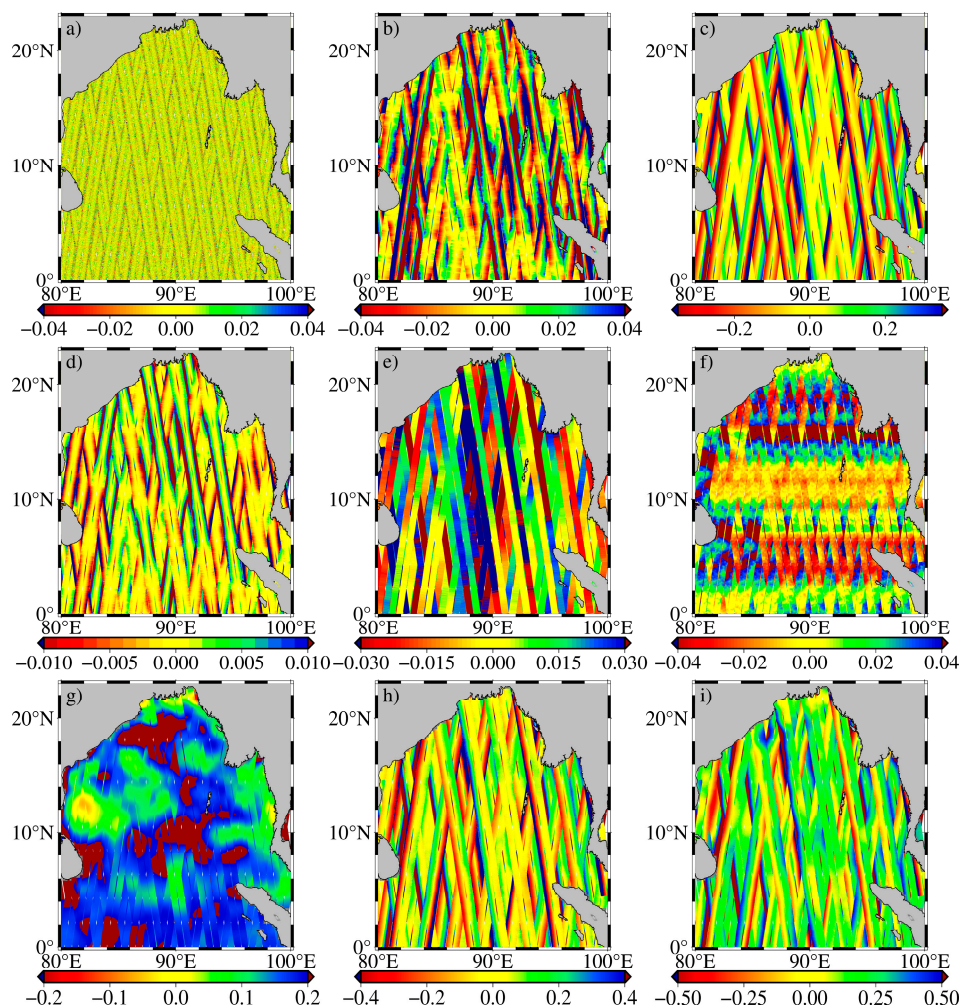


Figure 2. The distribution of errors in one cycle and the SLA data. (a) KaRIn error, (b) roll error, (c) phase error, (d) baseline dilation error, (e) timing error, (f) wet troposphere error, (g) original SLA data, (h) all errors, (i) SLA data with all errors.

The distribution of KaRIn error displays noticeable randomness. The roll error increases in the across-track direction as the distance to the nadir altimeter increases. The value of the roll error on both sides of the swath is opposite. The value of phase error is randomly distributed in the across-track direction and slowly changes in the along-track direction. The value of baseline dilation error is square distributed in the across-track direction [23,50]. The value of timing error is constant in the across-track direction and slowly changes in the along-track direction [22]. The value of wet troposphere error is affected by its spatial and temporal distribution, and the regularity of distribution in the along-track and across-track direction is not obvious. Table 2 provides statistical values of simulated errors in one cycle.

Table 2. The statistical values of simulated errors and total error in one cycle (Units: cm).

Error	Min	Max	Mean	STD
KaRIn	−9.3	9.8	1.1×10^{-5}	1.2
Roll	−16.5	15.1	-1.0×10^{-2}	3.4
Phase	−91.9	92.3	−0.6	22.2
Baseline dilation	−3.0	3.3	3.0×10^{-2}	0.6
Timing	−5.4	6.9	0.3	2.2
Wet troposphere	−6.6	6.9	0.7	2.4
All	−94.3	98.9	0.4	23.0

As shown in Table 2, phase error has the largest standard deviation (STD), and baseline dilation error has the smallest STD. The STD of KaRIn error is similar to that of timing error and wet troposphere error.

When a satellite flies from south to north, it is called an ascending orbit. When it flies from north to south, it is called a descending orbit. We need to analyze whether the distribution of errors on the ascending and descending orbits is the same. The errors on the ascending and descending orbits within one cycle are plotted separately (as shown in Figure 3) to study their differences.

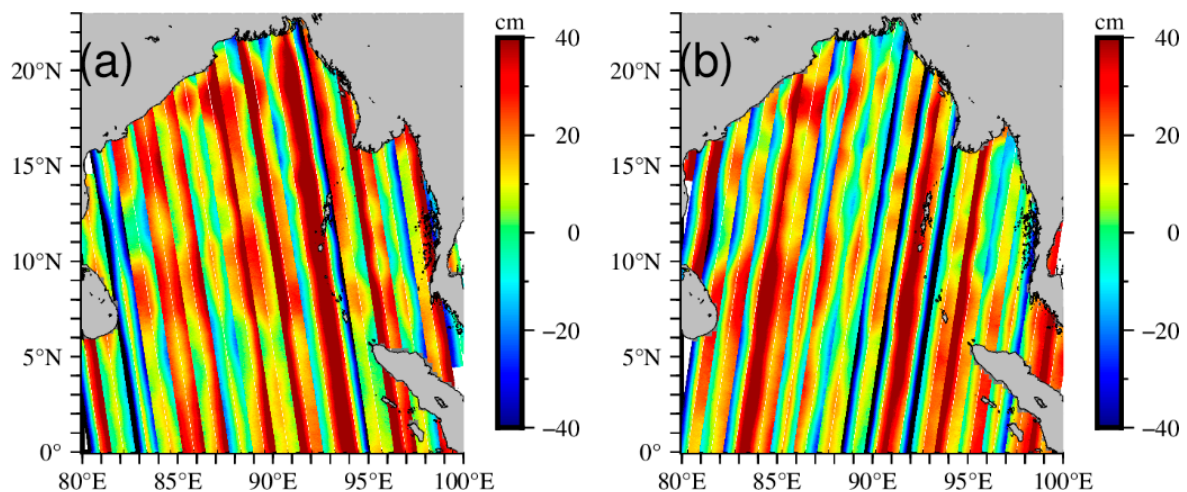


Figure 3. The distribution of one-cycle errors on ascending and descending passes. (a) Errors in descending passes, (b) errors in ascending passes.

It is clear from Figure 3 that the error fields have some distinction between ascending and descending orbits. Therefore, when processing data, it is necessary to calculate DOV and GA using the SSH data from ascending and descending orbits, respectively, then calculate the averaged DOV and GA, and finally calculate the SWOT_GGT by the averaged value (results are shown in Section 4).

3. Methodology

Based on the data processing experience from many scholars, the wide-swath data can be split into along-track and across-track directions [20,23,24]. The geoid gradients are calculated by utilizing information from adjacent points in multiple directions (as shown in Figure 4).

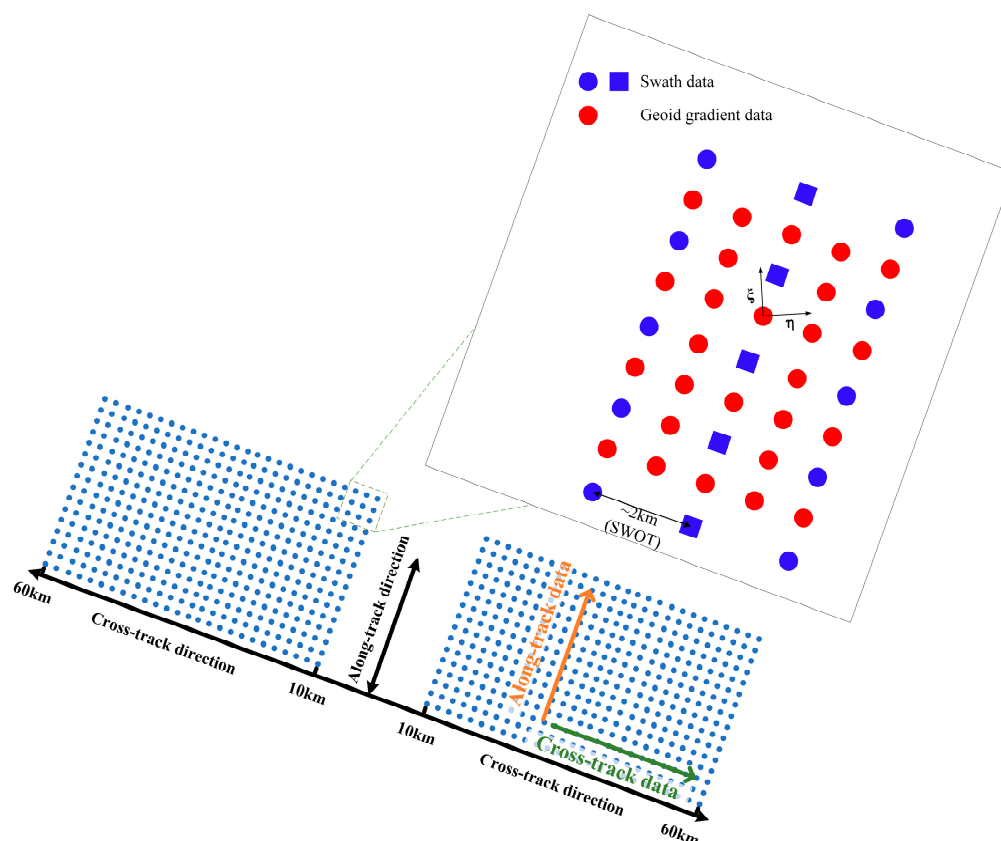


Figure 4. Split wide-swath data into along-track and across-track directions.

In Figure 4, the blue dots (the shape of the blue circle and the blue square has no special meaning, just to distinguish between the adjacent two columns of SSH grid data) represent SSH grid data, and the interval is 2 km. The red dots represent the geoid gradient calculated from the blue dots. We split the blue dots along-track and across-track to obtain one-dimensional observations separately, and then integrate these data across both the along-track and across-track directions to obtain one-dimensional cross-combined data. Around the blue dot, red dots can be calculated from the cross-combined data in multiple directions, then they can be used for the calculation of DOV. The two components, ξ and η , are used here only to indicate directions of partial derivatives of the geoid height, do not define a coordinate system.

In this study, the least-squares collocation (LSC) method is employed to compute DOV [51–53]. The obtained DOV is used in conjunction with the IVM formula to calculate GA [54,55]. The results are then utilized in the discretization method to calculate SWOT_GGT. This paper pays more attention to the impact of instrument errors on gravity gradients, so the introduction of LSC and IVM are placed in Appendix A; the results of the calculated DOV and GA are placed in Appendix B. The error propagation law of SWOT_GGT calculated by the DOV and GA is shown in Appendix C.

The relationship between the full tensor of gravity gradients, geoid heights, and DOV can be expressed in the local NEU frame:

$$\begin{cases} T_{xx} = \frac{\partial^2 T}{\partial x^2} = \gamma \frac{\partial^2 N}{\partial x^2} = \gamma \frac{\partial \xi}{\partial x} \\ T_{yy} = \frac{\partial^2 T}{\partial y^2} = \gamma \frac{\partial^2 N}{\partial y^2} = \gamma \frac{\partial \eta}{\partial y} \\ T_{zz} = -\frac{\partial^2 T}{\partial x^2} - \frac{\partial^2 T}{\partial y^2} = -\gamma \frac{\partial \xi}{\partial x} - \gamma \frac{\partial \eta}{\partial y} \\ T_{xy} = \frac{\partial^2 T}{\partial x \partial y} = \gamma \frac{\partial^2 N}{\partial x \partial y} = \gamma \frac{\partial \xi}{\partial y} = \gamma \frac{\partial \eta}{\partial x} \\ T_{xz} = \frac{\partial^2 T}{\partial x \partial z} = \frac{\partial \delta g}{\partial x} \\ T_{yz} = \frac{\partial^2 T}{\partial y \partial z} = \frac{\partial \delta g}{\partial y} \end{cases} \quad (1)$$

where γ represents the mean of the Earth’s normal gravity. The two components, ξ and η , are the partial derivatives of the geoid height N in the north–south and east–west directions, respectively. The formula is as follows:

$$\begin{cases} \xi = \frac{\partial N}{\partial x} = \frac{1}{R} \frac{\partial N}{\partial \varphi} \\ \eta = \frac{\partial N}{\partial y} = \frac{1}{R \cos \varphi} \frac{\partial N}{\partial \lambda} \end{cases} \quad (2)$$

where R is the average radius of the Earth, $R = 6,371,009$ m. If we express the full tensor of gravity gradients using the two components of DOV, it can be expressed as follows:

$$\begin{cases} T_{xx} = \frac{\gamma}{R^2} \frac{\partial^2 N}{\partial \varphi^2} + \frac{1}{R} \frac{\partial T}{\partial r} = \frac{\gamma}{R} \frac{\partial \xi}{\partial \varphi} + \frac{\delta g}{R} \\ T_{yy} = \frac{\gamma}{R^2 \cos^2 \varphi} \frac{\partial^2 N}{\partial \lambda^2} - \frac{\gamma \tan \varphi}{R^2} \frac{\partial N}{\partial \varphi} + \frac{\gamma}{R} \frac{\partial N}{\partial R} \\ = \frac{\gamma}{R \cos \varphi} \frac{\partial \eta}{\partial \lambda} - \frac{\gamma \tan \varphi}{R} \xi + \frac{\delta g}{R} \\ T_{zz} = -T_{xx} - T_{yy} \\ T_{xy} = \frac{\gamma}{R} \frac{1}{R \cos \varphi} \frac{\partial^2 N}{\partial \lambda \partial \varphi} + \frac{\sin \varphi}{R^2 \cos^2 \varphi} \delta g \\ = \frac{\gamma}{R} \frac{\partial \eta}{\partial \varphi} + \frac{\sin \varphi}{R^2 \cos^2 \varphi} \delta g = \frac{\gamma}{R \cos \varphi} \frac{\partial \xi}{\partial \lambda} + \frac{\sin \varphi}{R^2 \cos^2 \varphi} \delta g \\ T_{xz} = \frac{1}{R} \frac{\partial \delta g}{\partial \varphi} - \frac{\gamma}{R^2} \frac{\partial N}{\partial \varphi} = \frac{1}{R} \frac{\partial \delta g}{\partial \varphi} - \frac{\gamma}{R} \xi \\ T_{yz} = \frac{1}{R \cos \varphi} \frac{\partial \delta g}{\partial \lambda} - \frac{1}{R^2 \cos \varphi} \delta g \end{cases} \quad (3)$$

It is important to note that the calculated Δg needs to be converted to gravity disturbance data, δg . This conversion requires subtracting the correction terms, and the relationship between them is described as follows [56,57]:

$$\Delta g(x, y) = \delta g(x, y) - 2 \frac{\gamma}{R} N(x, y) \quad (4)$$

where N denotes the height of the geoid, and the correction term can be approximated as $-0.3076N$ mGal.

Transforming Equation (3) into a discretization equation yields [29]:

$$\begin{cases} T_{xx}(i, j) = \frac{\gamma}{R} \frac{\xi_{(i+1, j)} - \xi_{(i-1, j)}}{\varphi_{(i+1, j)} - \varphi_{(i-1, j)}} + \frac{\delta g_{(i, j)}}{R} \\ T_{yy}(i, j) = \frac{\gamma}{R \cos \varphi_{(i, j)}} \frac{\eta_{(i, j+1)} - \eta_{(i, j-1)}}{\lambda_{(i, j+1)} - \lambda_{(i, j-1)}} - \frac{\gamma \tan \varphi_{(i, j)}}{R} \xi_{(i, j)} + \frac{\delta g_{(i, j)}}{R} \\ T_{zz}(i, j) = -T_{xx}(i, j) - T_{yy}(i, j) \\ T_{xy}(i, j) = \frac{\gamma}{R \cos \varphi_{(i, j)}} \frac{\xi_{(i, j+1)} - \xi_{(i, j-1)}}{\lambda_{(i, j+1)} - \lambda_{(i, j-1)}} + \frac{\sin \varphi_{(i, j)}}{R^2 \cos^2 \varphi_{(i, j)}} \delta g_{(i, j)} \\ T_{xz}(i, j) = \frac{1}{R} \frac{\delta g_{(i+1, j)} - \delta g_{(i-1, j)}}{\varphi_{(i+1, j)} - \varphi_{(i-1, j)}} - \frac{\gamma}{R} \xi_{(i, j)} \\ T_{yz}(i, j) = \frac{1}{R \cos \varphi_{(i, j)}} \frac{\delta g_{(i, j+1)} - \delta g_{(i, j-1)}}{\lambda_{(i, j+1)} - \lambda_{(i, j-1)}} - \frac{1}{R^2 \cos \varphi_{(i, j)}} \delta g_{(i, j)} \end{cases} \quad (5)$$

Based on simulated SSH data, DOV and GA can be calculated using Equations (A1)~(A5) in Appendix A. Finally, the SWOT_GGT can be computed using Equation (5).

4. Results and Analysis

4.1. Validation of the Inversion Method of Full Tensor of Gravity Gradients

Before calculating SWOT_GGT, it is essential to check the reliability of the discretization method presented in Equation (5). For this purpose, we simulate gravity field data for part of the research region (10° – 13° N, 80° – 83° E) using EGM2008 [47] and XGM2019e models [43] based on the spherical harmonic expanded to degree and order 2190. In this validation, from the XGM2019e model, we can obtain the disturbance potential, DOV, and full tensor of gravity disturbance gradients (used as the truth value). The EGM2008 model is used as the reference gravity field model in the validation procedure. The differences between the true value and calculated value are shown in Table 3, where the “Ratio” represents the ratio between the STD of validation residuals and the STD of true values.

Table 3. The statistics of validation.

Component	Min (E)	Max (E)	Mean (E)	STD (E)	Ratio (%)
T_{xx}	−0.16	0.16	0.05	0.03	0.84
T_{yy}	−4.19	3.40	0.12	0.13	1.90
T_{zz}	−3.46	4.20	0.15	0.24	2.74
T_{xy}	−2.68	1.59	0.17	0.14	4.88
T_{xz}	−1.76	0.72	0.10	0.11	2.45
T_{yz}	−4.15	2.47	0.03	0.18	2.30

According to Table 3, all components exhibit a high level of accuracy, except for the T_{zz} component indicating relatively poorer performance with the STD of residuals reaching 0.24 E. The ratio indicates that the recovery error of each component is lower than 4.9%. The results demonstrate that the discretization method is reliable for inverting the full tensor of gravity gradients.

4.2. Full Tensor of Gravity Gradients Recovery from Simulated SWOT KaRIn Data

Using swot_simulator-1.2.4, we simulated one-cycle SSH data from 1–21 January 2021. The simulated data incorporate instruments and wet troposphere errors.

4.2.1. Results of SWOT_GGT

SWOT_GGT is calculated using the discretization method based on DOV and GA. The results of the SWOT_GGT by distinguishing SSH data in the ascending and descending orbits (proposed in Section 2) are shown in Table 4. The SWOT_GGT is plotted as shown in Figure 5.

In Table 4, T_{zz} exhibits the largest STD value, and T_{xy} shows the smallest STD value. The accuracy of the SWOT_GGT can be derived from the error propagation law shown in Appendix C. The error propagation law shows that the results in Table 4 are reliable. The data processing strategy proposed in Section 2 is also used in Section 5 to suppress errors more effectively.

Table 4. The statistics of SWOT_GGT (Unit: E).

Component	Mean	STD	RMS
T_{xx}	−0.06	10.97	10.97
T_{yy}	−0.13	15.92	15.92
T_{zz}	−0.14	22.04	22.04
T_{xy}	0.14	7.52	7.52
T_{xz}	−0.04	11.66	11.66
T_{yz}	−0.15	15.69	15.69

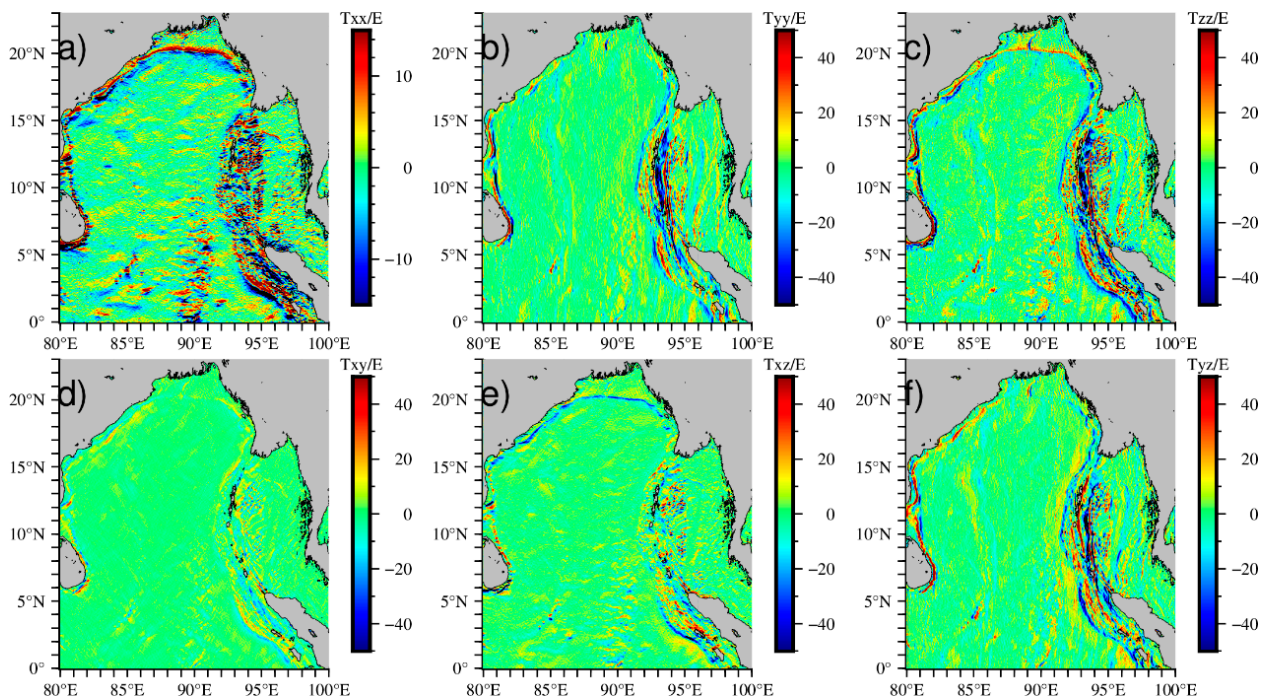


Figure 5. The SWOT_GGT derived from wide-swath data. (a) T_{xx} , (b) T_{yy} , (c) T_{zz} , (d) T_{xy} , (e) T_{xz} , (f) T_{yz} (Unit: E).

Combined with the seafloor topography (as shown in Figure 1), it can be found that the changes in Figure 5 are more obvious in the regions with drastic topographic changes, such as the near-shore region, the Burma Plate, the Sunda Plate, and around the 90°E ridge. The T_{zz} component in the above regions is the most obvious. The differences between the flat seafloor region and the drastic changes region are the largest. The T_{xy} component is the least sensitive to the gravity changes caused by topography. The remaining four components have no significant obvious changes except in the Burma Plate and its surrounding areas.

4.2.2. Precision of T_{zz} Component of the SWOT_GGT Evaluated by SIO

Currently, there are no available measurements of full tensor of gravity gradients in the BOB. The *curv_32.1* provided by SIO [44] is used to validate the precision of the T_{zz} component of the SWOT_GGT. In addition, GrafLab_GGT can help us to validate the all components of SWOT_GGT. The results of verifying the T_{zz} component are shown in this subsection. The results of evaluating all components of the SWOT_GGT are shown in the next subsection.

Except for validating the accuracy of the T_{zz} component of SWOT_GGT using the *curv_32.1* model, one can also assess the accuracy of the T_{zz} component of GrafLab_GGT using the same model. This approach provides an alternative means to evaluate the precision of GrafLab_GGT by focusing on the accuracy of T_{zz} component. By subtracting the T_{zz} component of SWOT_GGT from the *curv_32.1* model, the differences are obtained. Similarly, the T_{zz} component of GrafLab_GGT can be subtracted from the *curv_32.1* model to obtain differences. The results are shown in Figure 6. The statistical results are shown in Table 5.

It can be noted that the differences between the T_{zz} component of the SWOT_GGT and *curv_32.1* are concentrated in the Sunda Plate, the junction of the Indian and Burma Plates, and the junction of the Burma and Sunda Plates. In addition, large differences are also found in the northern part of the Bay of Bengal Basin, and the eastern and northern parts of the Sunda Plate. The positions are bordered by land. It is difficult to find differences between the two figures from Figure 6, which proves that the T_{zz} components of the SWOT_GGT and the GrafLab_GGT basically have the same accuracy.

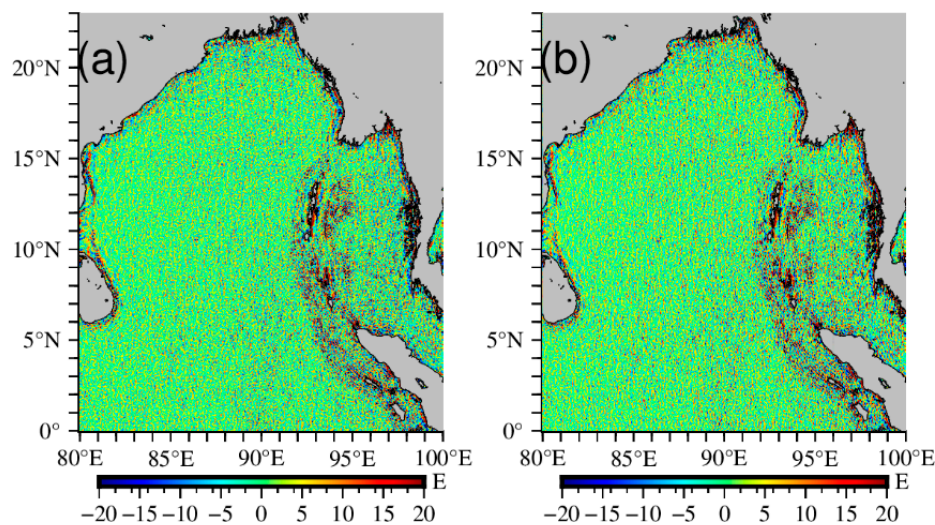


Figure 6. The results of validation: (a) validation of T_{zz} component of the SWOT_GGT by curv_32.1, (b) validation of T_{zz} component of the GrafLab_GGT by curv_32.1.

Table 5. The statistics of validation of T_{zz} component (Unit: E).

Component	Min	Max	Mean	STD	RMS
curv_32.1-SWOT_GGT T_{zz}	-335.51	209.32	0.17	8.67	8.68
curv_32.1-GrafLab_GGT T_{zz}	-335.09	209.25	0.31	8.96	8.96

As shown in Table 5, the RMS of the differences between the T_{zz} component of SWOT_GGT and curv_32.1 is 8.68 E. The RMS of the differences between the T_{zz} component of GrafLab_GGT and curv_32.1 is 8.96 E.

4.2.3. Precision of Full Components of SWOT_GGT Evaluated by GrafLab-Derived Results

The GrafLab_GGT is presented in Figure 7, and the statistics of each component of the GrafLab_GGT are presented in Table 6.

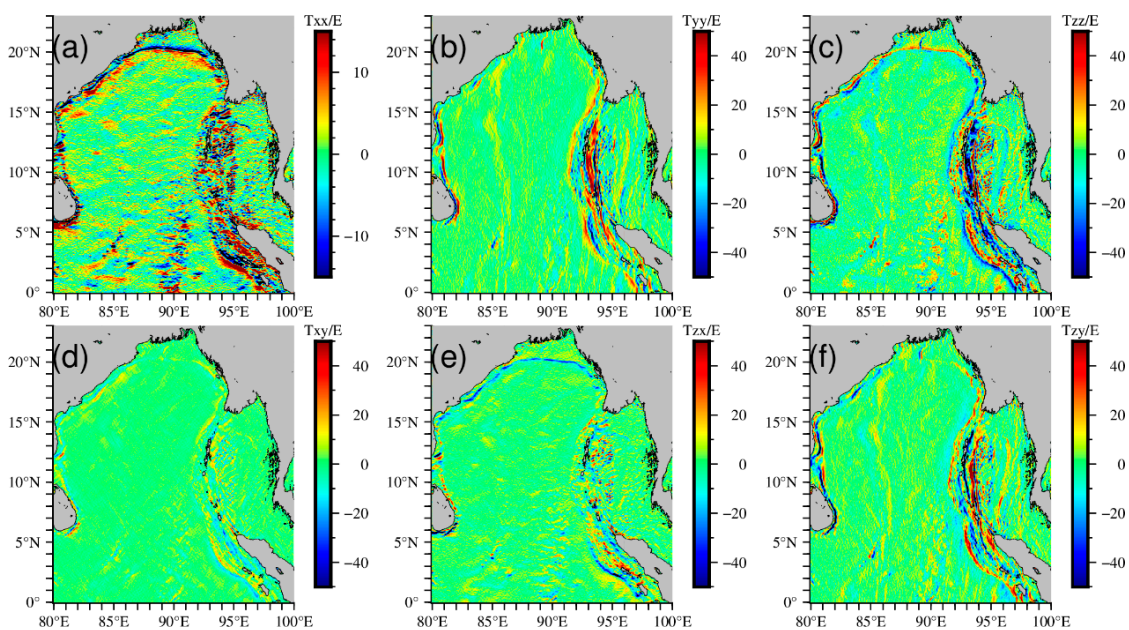


Figure 7. The GrafLab_GGT: (a) T_{xx} , (b) T_{yy} , (c) T_{zz} , (d) T_{xy} , (e) T_{xz} , (f) T_{yz} (Unit: E).

Table 6. The statistics of GrafLab_GGT (Unit: E).

Component	Min	Max	Mean	STD	RMS
T_{xx}	−222.30	189.63	0.09	11.06	11.06
T_{yy}	−248.27	216.47	−0.16	15.89	15.89
T_{zz}	−288.24	400.85	−0.25	22.08	22.08
T_{xy}	−128.24	147.97	0.13	7.46	7.46
T_{xz}	−214.46	220.44	−0.05	13.35	13.35
T_{yz}	−224.30	267.16	−0.28	17.56	17.56

Juxtaposing Figure 7 with Table 6, it can be found that the RMS of T_{zz} is the largest, about 22 E. The RMS of T_{xx} , T_{xz} , T_{yy} , and T_{yz} are similar. The RMS of T_{xy} is the smallest, about 7 E. Using GrafLab_GGT to validate SWOT_GGT, the results are presented in Table 7.

Table 7. The statistics of validation of SWOT_GGT by GrafLab_GGT (Unit: E).

Component	Min	Max	Mean	STD	RMS
T_{xx}	−39.44	53.96	0.01	3.17	3.17
T_{yy}	−53.42	62.55	0.01	4.21	4.21
T_{zz}	−78.55	116.48	0.12	5.99	5.99
T_{xy}	−34.00	28.53	0.01	2.01	2.01
T_{xz}	−85.94	85.92	0.01	5.61	5.61
T_{yz}	−53.55	53.83	0.03	5.78	5.78

In Table 7, it can be seen that the T_{zz} of the SWOT_GGT has the lowest precision, the RMS of the differences is 5.99 E. T_{xy} has the highest precision, the RMS of the differences is 2.01 E.

4.3. Impact of Instrument Errors on the Calculation of Full Tensor of Gravity Gradients

The schemes of experiments are shown in Table 8. To analyze the impact of instrument errors on the recovery of SWOT_GGT. Set the results of Scheme 1 as the true values, and the results of other schemes are compared with Scheme 1.

Table 8. Schemes of the effects of errors on SWOT_GGT computation.

Scheme	Content
1	SSH + no error
2	SSH + KaRIn error
3	SSH + roll error
4	SSH + phase error
5	SSH + baseline dilation error
6	SSH + timing error
7	SSH + wet troposphere error
8	SSH + all error

Calculating SWOT_GGT according to various schemes presented in Table 8; indeed, the results of Scheme 8 are presented in Section 4. The results of Scheme 1 are shown in Figure 8. The statistical results are presented in Table 9. The comparison results between Schemes 2~8 and Scheme 1 are presented in Figure 9.

Table 9. The statistics of SWOT_GGT calculated by Scheme 1 (Unit: E).

Component	Min	Max	Mean	STD	RMS
T_{xx}	−188.05	222.59	−0.17	10.38	10.38
T_{yy}	−215.61	245.18	−0.66	15.27	15.29
T_{zz}	−285.11	395.59	−0.98	21.19	21.21
T_{xy}	−128.88	147.41	0.15	6.86	6.86
T_{xz}	−184.25	154.22	−0.27	11.26	11.26
T_{yz}	−209.61	199.88	−0.91	15.08	15.11

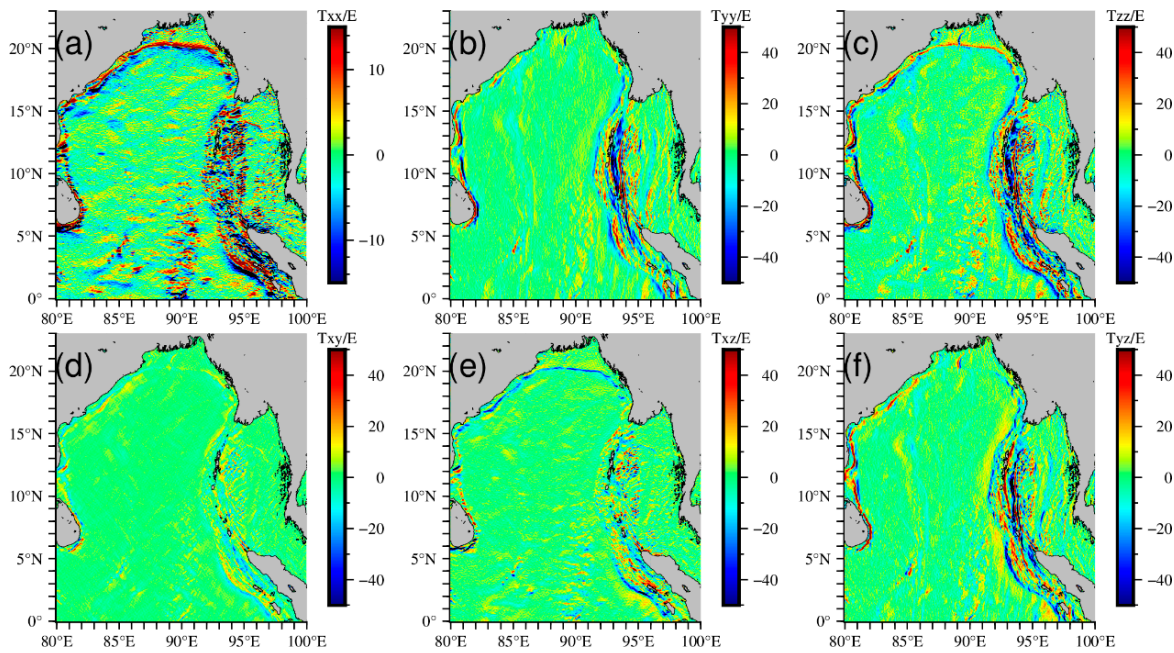


Figure 8. The SWOT_GGT calculated by Scheme 1: (a) T_{xx} , (b) T_{yy} , (c) T_{zz} , (d) T_{xy} , (e) T_{xz} , (f) T_{yz} (Unit: E).

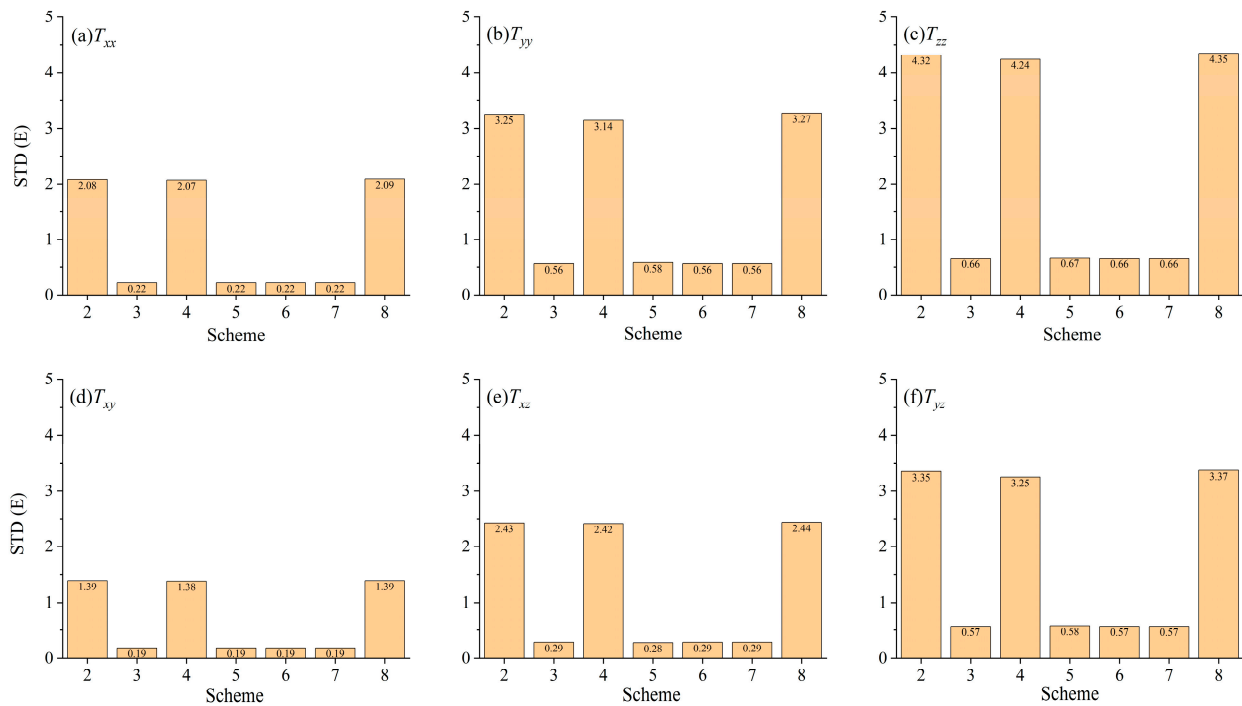


Figure 9. The comparison results compared with Scheme 1: (a) T_{xx} , (b) T_{yy} , (c) T_{zz} , (d) T_{xy} , (e) T_{xz} , (f) T_{yz} (Unit: E).

In Figure 9, as the mean of the verification residuals for each component is around 10^{-4} E, so the mean is not plotted. Only the STD is shown. For ease of comparison, the maximum value of the Y-axis in each subplot is set to 5 E. As shown in Figure 9, the poorest and best performances are observed in T_{zz} and T_{xy} components, respectively. This indicates that the various errors have the greatest impact on the T_{zz} component and the least impact on the T_{xy} component of the SWOT_GGT. Comparing the results of different schemes, it is evident that the inclusion of KaRIn error and phase error significantly affect

the computation of the SWOT_GGT. These two errors dominate the statistics of the total error impact in Scheme 8.

The remaining four errors have relatively minor effects on the computation of the SWOT_GGT. Taking the results of Scheme 2 and Scheme 7 as examples, the inclusion of the KaRIn error results in an impact of 4.32 E on the T_{zz} component, while the inclusion of wet troposphere error only causes a minor impact of 0.66 E on the same component (Figure 9c). Similarly, the inclusion of the KaRIn error leads to an impact of 1.39 E on the T_{xy} component, whereas the inclusion of the wet troposphere error results in a smaller impact of 0.19 E on the same component (Figure 9d).

In Figure 9, it can be seen that the results of Scheme 8 are not a simple mathematical accumulation of the results from Scheme 2 to Scheme 7. The phenomenon is evident because the STD of residuals is not zero in other schemes. This may be attributed to the presence of correlations among the various errors introduced in these experiments.

5. Discussion

Yu et al. [20] and Ma et al. [23] have shown that the GA calculated using multi-cycle SSH data is better than that calculated using only one cycle. To analyze the effect of multi-cycle on the calculation of SWOT_GGT, 19 cycles of SSH data are prepared. The errors of the ascending and descending orbits within 19 cycles are plotted separately in Figure 10.

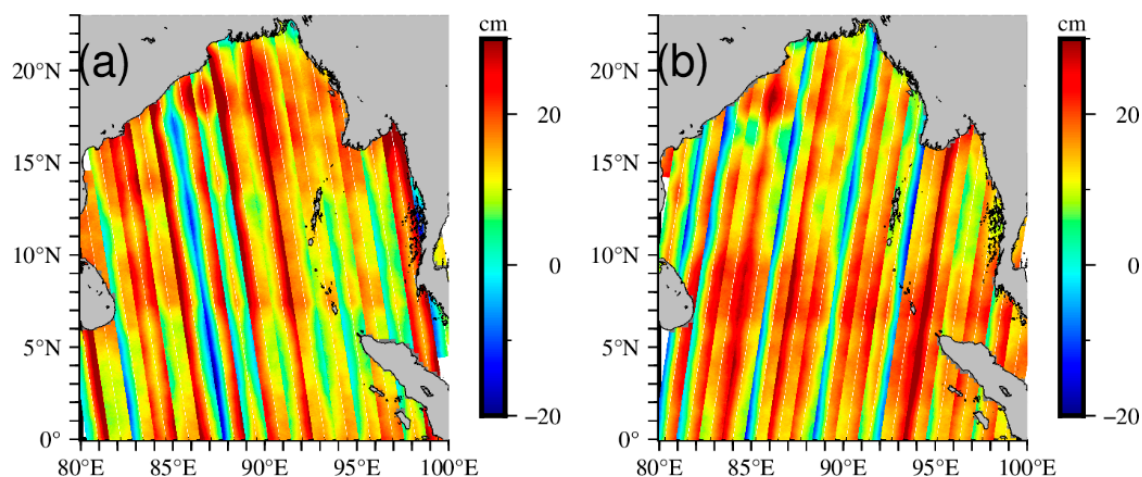


Figure 10. The distribution of 19-cycle errors in ascending and descending passes. (a) Errors in descending passes. (b) errors in ascending passes.

From Figure 10, we can see that 19-cycle errors are significantly smaller compared with Figure 3. This indicates that it is necessary to process SSH data for ascending and descending orbits separately mentioned in Section 2.

We calculate the STD of the differences between errors simulated for 19 cycles and 1 cycle. The results are plotted in Figure 11, where the “Ratio” indicates the ratio of the error weakened by 19 cycles of data relative to 1 cycle of data.

The comparison shows that multi-cycle data can effectively eliminate errors. The suppression of the KaRIn, roll, phase, baseline dilation, and timing errors is obvious. The reduction in timing error is greater than 69%. In contrast, the wet troposphere error has not changed significantly, and multiple cycles only reduce the error by 2.92%, which may be related to its characteristics of uneven temporal and spatial distribution [58].

To compare the effects of multi-cycle data on the recovery of SWOT_GGT, another experiment is conducted. The result obtained from one-cycle data is abbreviated as Plan A. The result obtained from 19-cycle data is referred to as Plan B. The results of both plans are calculated based on data that distinguish between ascending and descending orbits. The validation results of the two plans are presented in Figure 12. The “Ratio” indicates the ratio of precision improved by Plan B relative to Plan A.

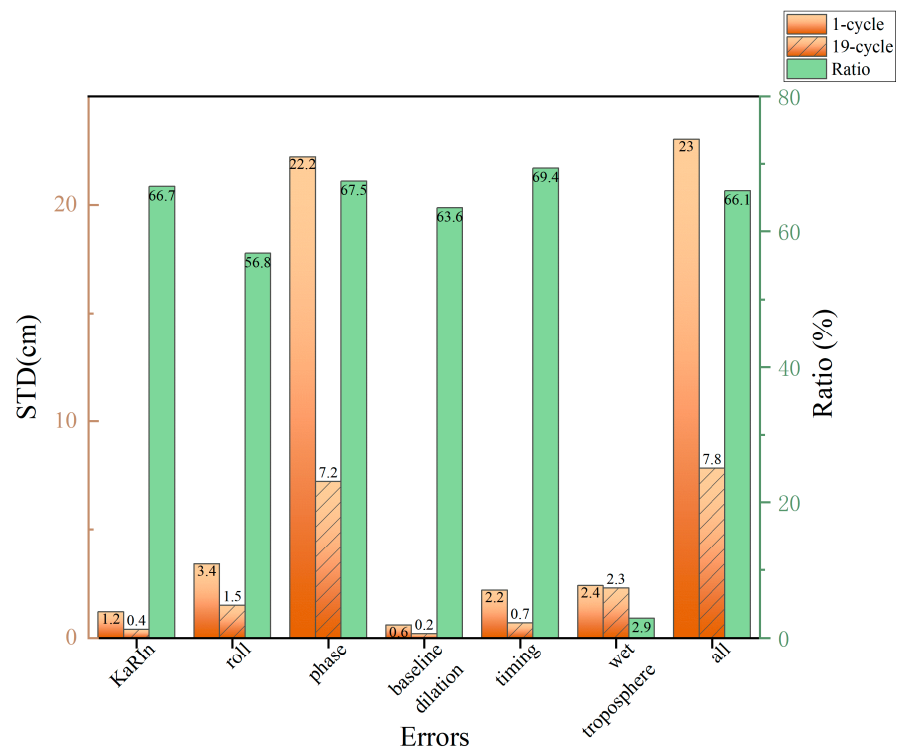


Figure 11. The comparison between 1-cycle errors and 19-cycle errors.

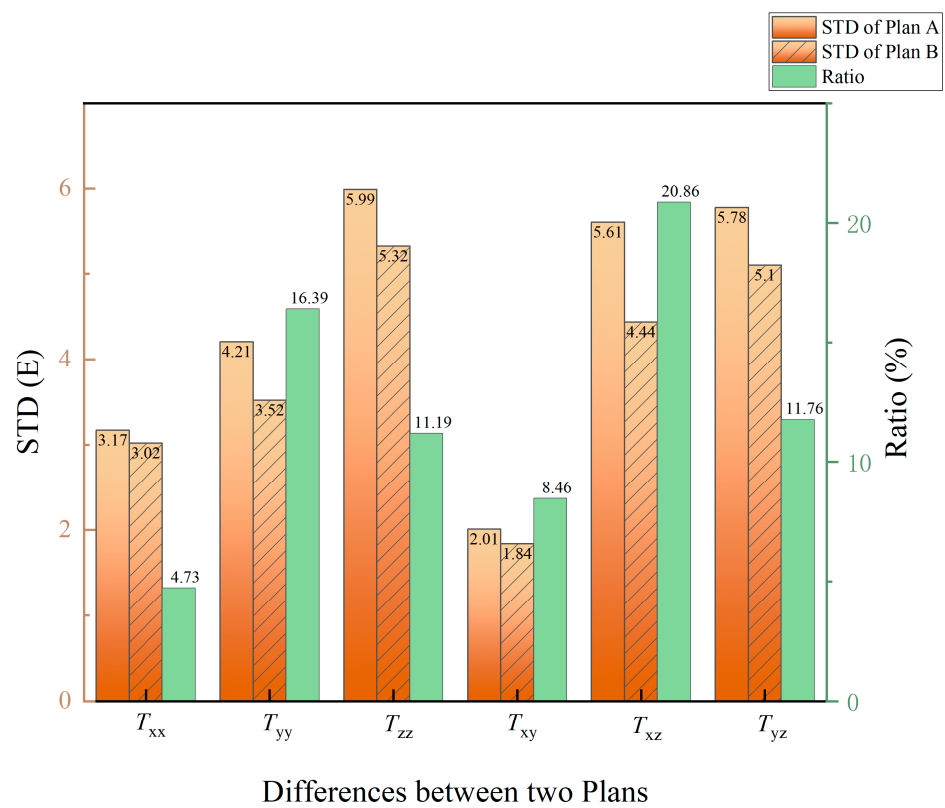


Figure 12. Statistics of differences of SWOT_GGT between Plan A and Plan B.

By comparing the statistics, it is found that the precision of the results recovered from 19 cycles of data is better than that from 1 cycle of data. The SWOT_GGT obtained from the two plans has the same feature, i.e., the T_{zz} component has the lowest precision. This may

be due to the fact that the T_{zz} component is derived by T_{xx} and T_{yy} ; according to the error propagation law shown in Appendix C, T_{zz} would have a larger error than T_{xx} and T_{yy} .

As shown in Figure 12, compared with the SWOT_GGT recovered by Plan A, the precision of the T_{yy} , T_{zz} , T_{xz} , and T_{xy} components of Plan B is improved significantly, by more than 11%. Experiments show that multi-cycle data can significantly reduce the influence of instrument errors on the full tensor of gravity gradients calculated by the discretization method.

The current experiments are based on simulated data, where we simulated instrument errors and investigated the impact of multi-cycle data on suppressing these errors when inverting gravity gradients tensor. From Figures 11 and 12, it is evident that multi-cycle data effectively mitigate instrument errors. However, numerical simulations cannot substitute real measured data. SWOT is influenced by various factors during actual operation, such as ocean tides, which were not considered in our experiments. Therefore, with the release of “Pre-Validated” data in the future, our experiments will be based on real measurements to obtain gravity gradients and assess their accuracy.

6. Conclusions

To evaluate the possible precision of gravity gradient recovery from SWOT data, this study used the discretization method to compute SWOT_GGT. The T_{zz} component of the SWOT_GGT is validated by curv_32.1. The RMS of the differences is about 8.68 E. The full components of the SWOT_GGT are validated by GrafLab_GGT. The results show that the precision of the T_{zz} component is the lowest. The RMS of differences is 5.99 E. The precision of the T_{xy} component is the highest. The RMS of differences is 2.01 E. The results reveal that the KaRIn error and phase error have a significant impact on the SWOT_GGT. The T_{zz} component of the SWOT_GGT is the most sensitive to the effects of errors, while the T_{xy} component is the least sensitive one. A comparison between SWOT_GGT calculated using 1 cycle of data and 19 cycles of data indicates that the SWOT_GGT recovered from multi-cycle data is less affected by instrument errors. These results demonstrate that SWOT can help us obtain full tensor of gravity gradients with precision better than 10 E at least.

The SWOT mission provides a possible means to enhance the accuracy of ocean gravity field products via two-dimensional SSH observations. However, according to the results of this study, instrument errors can largely influence the precision of the recovered gravity gradients. Therefore, with the release of SWOT’s “Pre-Validated” science data in the near future, it is key to investigate ways, such as the crossover calibration method, discretization method, filtering method, etc., for processing the various errors caused by the interferometric radar altimeter.

Author Contributions: Conceptualization, H.G. and X.W.; methodology, X.W. and S.T.; validation, H.G. and X.W.; resources, H.G., F.W. and X.W.; data curation, X.W.; writing—original draft preparation, H.G.; writing—review and editing, X.W.; funding acquisition, X.W. All authors have read and agreed to the published version of the manuscript.

Funding: This research was funded by the National Natural Science Foundation of China (No. 42074017) and Key Laboratory of Smart Earth (No. KF2023YB01-12).

Data Availability Statement: The data underlying this article will be shared on reasonable request to the corresponding author.

Acknowledgments: We would like to thank SIO for providing the V32.1 models, DTU for providing the DTU21 bathymetric model, ESA for providing SLA data, and JPL for making the swot_simulator-1.2.4 available for this study. We are very grateful to Blažej Bucha for providing us the GrafLab-1.1.2 program. This research is supported by the National Natural Science Foundation of China (No. 42074017) and Key Laboratory of Smart Earth (No. KF2023YB01-12).

Conflicts of Interest: The authors declare no conflicts of interest.

Appendix A

The geoid gradient, e , and the residual DOV, ε , are computed based on the geoid heights between adjacent points and the spherical distance, ψ , between the two points:

$$e = -\varepsilon = \frac{\partial N}{\partial \psi} \quad (\text{A1})$$

The residual geoid gradient and residual DOV are calculated by subtracting the geoid gradients of the along-track and cross-track from the reference field.

The residual DOV is calculated by the LSC method [59,60]. The LSC combines the calculation and the grid transformation of DOV into one step:

$$\begin{pmatrix} \xi_{res} \\ \eta_{res} \end{pmatrix} = \begin{pmatrix} C_{\xi e} \\ C_{\eta e} \end{pmatrix} (C_{ee} + C_n)^{-1} e_{res} \quad (\text{A2})$$

where ξ_{res} and η_{res} are the north component and the east component of residual gridded DOV, respectively; $C_{\xi e}$ is the covariance matrix for the north component of gridded DOV and the residual geoid gradient, $C_{\eta e}$ is the covariance matrix for the prime vertical component of grid DOV and the residual geoid gradient; C_{ee} is the variance matrix for the gradient, C_n works as a filter and is a diagonal matrix containing the noise variances of geoid gradient, and e_{res} is the residual geoid gradient calculated by Equation (A1).

Using the IVM formula, select the appropriate kernel function, and solve for the GA based on the grid DOV [60,61]. The one-dimensional (1-D) FFT method and IVM formula are used to derive the GA from the DOV [60]. Since the difference in latitude is taken into account in the calculation of spherical latitude by the 1-D FFT method, the algorithm is more rigorous in theory [6]:

$$\Delta g(p) = \frac{\gamma_0}{4\pi} \iint_{\sigma} H'(\psi) (\xi_q \cos \alpha_{qp} + \eta_q \sin \alpha_{qp}) d\sigma_q \quad (\text{A3})$$

$H'(\psi)$ is the derivative of the kernel function:

$$H(\psi) = \frac{1}{\sin \frac{\psi}{2}} + \log \left(\frac{\sin^3 \frac{\psi}{2}}{1 + \sin \frac{\psi}{2}} \right) \quad (\text{A4})$$

where ψ is the spherical distance between point q and point p.

The ψ cannot be zero in the derivative of the kernel function, so it is necessary to consider the influence of the inner zone effect on GA derivation [36,60]:

$$\Delta g = \frac{s_0 \gamma_0}{2} (\xi_x + \eta_y) \quad (\text{A5})$$

where ξ_x and η_y are the change rates of the meridian and prime vertical component of the DOV, respectively; s_0 is the size of the inner zone. Δx and Δy are the distance of the grid, respectively. Finally, DOV and GA are restored using the XGM2019e.

Appendix B

Employing the LSC method, we restored DOV at a resolution of $1' \times 1'$ (as shown in Figure A1). Subsequently, utilizing the IVM formula, we computed GA at a resolution of $1' \times 1'$ (as shown in Figure A1).

The statistics of SWOT_DOV and SWOT_GA are presented in Table A1. The predicted precision of SWOT_DOV is validated by east_32.1 and north_32.1, and the SWOT_GA is validated by grav_32.1 and the NCEI shipborne gravity anomalies, respectively. The results are presented in Table A2.

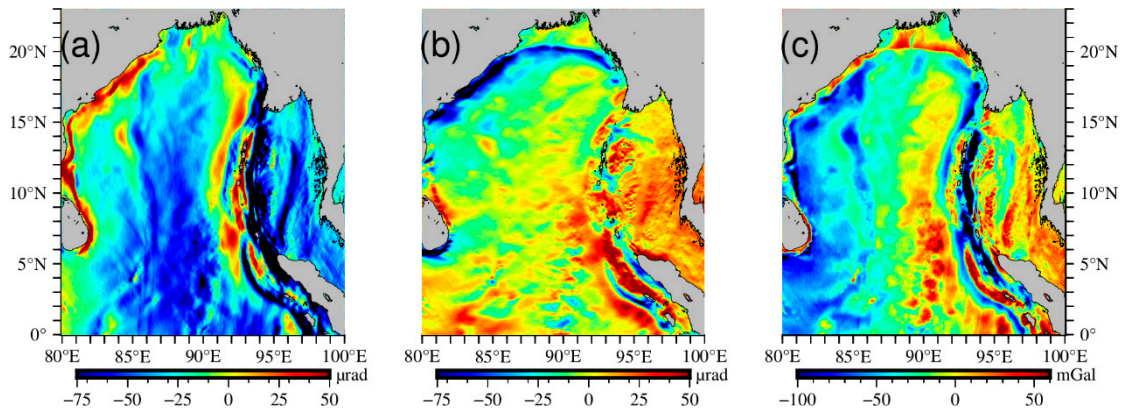


Figure A1. The DOV and the GA: (a) component η , (b) component ζ , (c) GA.

Table A1. The statistics of SWOT_DOV and SWOT_GA.

Component	Min	Max	Mean	STD
SWOT_DOV_N (μrad)	−176.96	186.44	−3.24	22.92
SWOT_DOV_E (μrad)	−243.95	187.27	−28.74	30.41
SWOT_GA (mGal)	−198.02	246.95	−16.88	35.32

Table A2. Validation of SWOT_DOV and SWOT_GA.

Component	Min	Max	Mean	STD
SWOT_DOV_N by north_32.1 (μrad)	−44.17	36.29	0.01	3.05
SWOT_DOV_E by east_32.1 (μrad)	−49.28	52.67	0.08	4.22
By grav_32.1 (mGal)	−93.41	55.91	0.12	5.05
By NCEI (mGal)	−29.95	30.08	0.12	5.09

The accuracy of SWOT_DOV derived from simulated wide-swath data is a little higher in the north–south direction than in the east–west direction. The STD of differences is 5.05 mGal compared to the grav_32.1 of SIO. The STD of differences between the SWOT_GA and NCEI shipborne gravity, particularly at the shipborne measurement points, is 5.09 mGal.

Appendix C

According to the error propagation law, the relationship between the full tensor of gravity gradients and DOV and GA can be determined:

$$\left\{ \begin{array}{l} \delta_{Txx}^2 = \frac{\partial T_{xx}}{\partial \zeta \partial g} = \frac{\gamma^2}{R^2} \frac{\delta \zeta^2}{\Delta \varphi^2} + \frac{\delta g^2}{R^2} \\ \delta_{Tyy}^2 = \frac{\partial T_{yy}}{\partial \eta \partial \zeta \partial g} = \frac{\gamma^2}{R^2 \cos^2 \varphi} \frac{\delta \eta^2}{\Delta \lambda^2} + \frac{\gamma^2 \tan^2 \varphi}{R^2} \delta \zeta^2 + \frac{\delta g^2}{R^2} \\ \delta_{Tyy}^2 = \delta_{Txx}^2 + \delta_{Tyy}^2 \\ \delta_{Txy}^2 = \frac{\partial T_{xy}}{\partial \eta \partial g} = \frac{\gamma^2}{R^2 \cos^2 \varphi} \frac{\delta \zeta^2}{\Delta \lambda^2} + \frac{\sin^2 \varphi}{R^4 \cos^4 \varphi} \delta g^2 \\ \delta_{Txz}^2 = \frac{\partial T_{xz}}{\partial \zeta \partial g} = \frac{1}{R^2} \frac{\delta g^2}{\Delta \varphi^2} - \frac{\gamma^2}{R^2} \delta \zeta^2 \\ \delta_{Tyz}^2 = \frac{\partial T_{yz}}{\partial g} = \frac{1}{R^2 \cos^2 \varphi} \frac{\delta g^2}{\Delta \lambda^2} - \frac{1}{R^4 \cos^2 \varphi} \delta g^2 \end{array} \right. \quad (\text{A6})$$

where $\Delta \varphi$ represents the grid distance in the north–south direction, $\Delta \lambda$ represents the grid distance in the east–west direction, φ represents latitude, and γ represents the normal gravity.

References

1. Hwang, C.; Tseng, T.P.; Lin, T.J.; Švehla, D.; Hugentobler, U.; Chao, F.B. Quality assessment of FORMOSAT-3/COSMIC and GRACE GPS observables: Analysis of multipath, ionospheric delay and phase residual in orbit determination. *GPS Solut.* **2010**, *14*, 121–131. [\[CrossRef\]](#)
2. Guo, J.Y.; Qin, J.; Kong, Q.L.; Li, G.W. On simulation of precise orbit determination of HY-2 with centimeter precision based on satellite-borne GPS technique. *Appl. Geophys.* **2012**, *9*, 95–107. [\[CrossRef\]](#)
3. Fenoglio-Marc, L.; Dinardo, S.; Uebbing, B.; Buchhaupt, C.; Gärtner, M.; Staneva, J.; Becker, M.; Klos, A.; Kusche, J. Advances in NE-Atlantic coastal Sea Level Change Monitoring from Delay Doppler Altimetry. *Adv. Space Res.* **2021**, *68*, 571–592. [\[CrossRef\]](#)
4. Andersen, O.B.; Knudsen, P.; Berry, P.M. The DNSCO8GRA global marine gravity field from double retracked satellite altimetry. *J. Geod.* **2010**, *84*, 191–199. [\[CrossRef\]](#)
5. Kaula, W.M. *Theory of Satellite Geodesy: Applications of Satellites to Geodesy*; Courier Corporation: Waltham, MA, USA, 1966.
6. Zhu, C.C.; Liu, X.; Guo, J.Y.; Yu, S.W.; Niu, Y.P.; Yuan, J.J.; Li, Z.; Gao, Y.G. Sea surface heights and marine gravity determined from SARAL/AltiKa Ka-band altimeter over South China Sea. *Pure Appl. Geophys.* **2021**, *178*, 1513–1527. [\[CrossRef\]](#)
7. Wan, X.Y.; Hao, R.J.; Jia, Y.J.; Wu, X.; Wang, Y.; Feng, L. Global marine gravity anomalies from multi-satellite altimeter data. *Earth Planets Space* **2022**, *74*, 165. [\[CrossRef\]](#)
8. Bao, L.F.; Xu, H.Z.; Li, Z.C. Towards a 1 mGal accuracy and 1 min resolution altimetry gravity field. *J. Geod.* **2013**, *87*, 961–969. [\[CrossRef\]](#)
9. Sandwell, D.T.; Mueller, R.D.; Smith, W.H.F.; Garcia, E.; Francis, R. New global marine gravity model from cryosat-2 and jason-1 reveals buried tectonic structure. *Science* **2014**, *346*, 65–67. [\[CrossRef\]](#)
10. Jin, T.Y.; Zhou, M.; Zhang, H.; Li, J.C.; Jiang, W.P.; Zhang, S.J.; Hu, M.Z. Analysis of vertical deflections determined from one cycle of simulated SWOT wide-swath altimeter data. *J. Geod.* **2022**, *96*, 30. [\[CrossRef\]](#)
11. Yuan, J.J.; Guo, J.Y.; Zhu, C.C.; Li, Z.; Liu, X.; Gao, J.Y. SDUST2020 MSS: A global $1' \times 1'$ mean sea surface model determined from multi-satellite altimetry data. *Earth Syst. Sci. Data Discuss* **2023**, *15*, 155–169. [\[CrossRef\]](#)
12. Zhu, F.S.; Liu, X.; Li, Z.; Yuan, J.J.; Guo, J.Y.; Sun, H.P. High spatial resolution marine gravity trend determined from multisatellite altimeter data over Bay of Bengal. *Geophys. J. Int.* **2023**, *25*, 2257–2267. [\[CrossRef\]](#)
13. Yang, J.J.; Jekeli, C.; Liu, L.T. Seafloor topography estimation from gravity gradients using simulated annealing. *J. Geophys. Res. Solid Earth* **2018**, *123*, 6958–6975. [\[CrossRef\]](#)
14. Annan, R.F.; Wan, X.Y. Recovering Bathymetry of the Gulf of Guinea Using Altimetry-Derived Gravity Field Products Combined via Convolutional Neural Network. *Surv. Geophys.* **2022**, *43*, 1541–1561. [\[CrossRef\]](#)
15. Wan, X.Y.; Annan, R.F.; Ziggah, Y.Y. Altimetry-derived Gravity Gradients using Spectral Method and Their Performance in Bathymetry Inversion using Back-Propagation Neural Network. *J. Geophys. Res. Solid Earth* **2023**, *128*, e2022JB025785. [\[CrossRef\]](#)
16. Liu, H.; Wu, L.; Bao, L.F.; Li, Q.Q.; Zhang, P.P.; Wang, Y. Gravity matching navigation algorithm based on multiscale search and Hadamard transformed difference. *ISA Trans.* **2022**, *128*, 409–422. [\[CrossRef\]](#)
17. Fu, L.-L.; Ubelmann, C. On the transition from profile altimeter to swath altimeter for observing global ocean surface topography. *J. Atmos. Ocean. Technol.* **2014**, *31*, 560–568. [\[CrossRef\]](#)
18. Wan, X.Y.; Jin, S.G.; Liu, B.; Tian, S.; Kong, W.Y.; Annan, R.F. Effects of InSAR Altimetry Errors on Marine Gravity Field Inversion. *Sensors* **2020**, *20*, 2465. [\[CrossRef\]](#)
19. Bruni, S.; Fenoglio-Marc, L.; Raicich, F.; Zerbini, S. On the consistency of coastal sea level measurements in the Mediterranean Sea from tide gauge and satellite altimetry. *J. Geod.* **2022**, *96*, 41. [\[CrossRef\]](#)
20. Yu, D.C.; Hwang, C.; Andersen, O.B.; Chang, E.T.Y.; Gaultier, L. Gravity recovery from SWOT altimetry using geoid height and geoid gradient. *Remote Sens. Environ.* **2021**, *265*, 112650. [\[CrossRef\]](#)
21. Fu, L.-L.; Pavelsky, T.; Morrow, R.; Cretaux, J.F.; Farrar, T. The SWOT (Surface Water and Ocean Topography) Mission and Its Status. In Proceedings of the EGU General Assembly 2023, Vienna, Austria, 24–28 April 2023; EGU23-17156. [\[CrossRef\]](#)
22. Esteban-Fernandez, D.; Fu, L.-L.; Pollard, B.; Vaze, P.; Abelson, R.; Steunou, N. *Swot Project: Mission Performance and Error Budget; Revision a*. Tech. Rep. JPL D-79084; Jet Propulsion Laboratory: Pasadena, CA, USA, 2017.
23. Ma, G.; Jin, T.Y.; Jiang, P.Y.; Shi, J.S.; Zhou, M. Calibration of the Instrumental Errors on Marine Gravity Recovery from SWOT Altimeter. *Mar. Geod.* **2023**, *46*, 496–522. [\[CrossRef\]](#)
24. Liu, X.; Song, M.H.; Li, C.; Hui, G.H.; Guo, J.Y.; Jia, Y.J.; Sun, H.P. Inversion method of deflection of the vertical based on SWOT wide-swath altimeter data. *Geod. Geodyn.* **2023**. [\[CrossRef\]](#)
25. Liu, X.; Hui, G.H.; Guo, J.Y.; Zhang, T.H.; Song, M.H. Inversion of Deflection of the Vertical in the South China Sea Using ICESat-2 Sea Surface Height Data. *Remote Sens.* **2023**, *15*, 30. [\[CrossRef\]](#)
26. Yu, D.C.; Hwang, C. Calibrating error variance and scaling global covariance function of geoid gradients for optimal determinations of gravity anomaly and gravity gradient from altimetry. *J. Geod.* **2022**, *96*, 61. [\[CrossRef\]](#)
27. Zhou, R.C.; Liu, X.; Li, Z.; Sun, Y.; Yuan, J.J.; Guo, J.Y.; Ardan, A.A. On performance of vertical gravity gradient determined from CryoSat-2 altimeter data over Arabian Sea. *Geophys. J. Int.* **2023**, *234*, 1519–1529. [\[CrossRef\]](#)
28. Wan, X.Y.; Wang, F.; Guo, H.Y.; Liu, B. Impact of Errors in Environmental Correction on Gravity Field Recovery Using Interferometric Radar Altimeter Observations. *Remote Sens.* **2022**, *14*, 6299. [\[CrossRef\]](#)
29. Tian, S. *Analysis of Interferometric Imaging Radar Altimeter Errors on Accuracy of Marine Gravity Field Inversion*; China University of Geosciences (Beijing): Beijing, China, 2019. [\[CrossRef\]](#)

30. Rummel, R.; Yi, W.Y.; Stummer, C. GOCE gravitational gradiometry. *J. Geod.* **2011**, *85*, 777–790. [[CrossRef](#)]
31. Zheleznyak, L.K.; Koneshov, V.N.; Mikhailov, P.S. Experimental determination of the vertical gravity gradient below the sea level. *Izv.-Phys. Solid Earth* **2016**, *52*, 866–868. [[CrossRef](#)]
32. Wan, X.; Yu, J. Navigation Using Invariants of Gravity Vectors and Gravity Gradients. In *China Satellite Navigation Conference (CSNC) 2014 Proceedings: Volume III*; Sun, J., Jiao, W., Wu, H., Lu, M., Eds.; Lecture Notes in Electrical Engineering; Springer: Berlin/Heidelberg, Germany, 2014; Volume 305. [[CrossRef](#)]
33. Wan, X.Y.; Ran, J.J.; Jin, S.G. Sensitivity analysis of gravity anomalies and vertical gravity gradient data for bathymetry inversion. *Mar. Geophys. Res.* **2019**, *40*, 87–96. [[CrossRef](#)]
34. Yu, J.H.; Xu, H.; Wan, X.Y. Curvilinear Coordinates from the Gravitational Field and the Related Application in Orientation and Navigation. *Acta Geod. Cartogr. Sin.* **2021**, *50*, 153–159.
35. Wan, X.Y.; Wang, H.B.; Jia, Y.J. Performance of Haiyang-2 Derived Gravity Field Products in Bathymetry Inversion. *Remote Sens.* **2023**, *15*, 32. [[CrossRef](#)]
36. Heiskanen, W.A.; Moritz, H. *Physical Geodesy*; Freeman WH: San Francisco, CA, USA, 1967.
37. Liu, B.; Bian, S.F.; Ji, B.; Wu, S.G.; Xian, P.F.; Chen, C.; Zhang, R.C. Application of the Fourier Series Expansion Method for the Inversion of Gravity Gradients using Gravity Anomalies. *Remote Sens.* **2023**, *15*, 230. [[CrossRef](#)]
38. Ji, H.; Guo, J.Y.; Zhu, C.C.; Yuan, J.J.; Liu, X.; Li, G.W. On Deflections of Vertical Determined From HY-2A/GM Altimetry Data in the Bay of Bengal. *IEEE J. Sel. Top. Appl. Earth Obs. Remote Sens.* **2021**, *14*, 12048–12060. [[CrossRef](#)]
39. Ji, H.; Liu, X.; Zhu, C.C.; Yuan, J.J.; Ji, B.; Guo, J.Y. On performance of CryoSat-2 altimeter data in deriving marine gravity over the Bay of Bengal. *Mar. Geophys. Res.* **2021**, *42*, 39. [[CrossRef](#)]
40. Taburet, G.; Sanchez-Roman, A.; Ballarotta, M.; Pujol, M.I.; Legeais, J.F.; Fournier, F.; Faugere, Y.; Dibarboure, G. DUACS DT2018: 25 years of reprocessed sea level altimetry products. *Ocean Sci.* **2019**, *15*, 1207–1224. [[CrossRef](#)]
41. Pujol, M.; Schaeffer, P.; Faugère, Y.; Raynal, M.; Dibarboure, G.; Picot, N. Gauging the improvement of recent mean sea surface models: A new approach for identifying and quantifying their errors. *J. Geophys. Res. Ocean.* **2018**, *123*, 5889–5911. [[CrossRef](#)]
42. Mulet, S.; Rio, M.H.; Etienne, H.; Artana, C.; Cancet, M.; Dibarboure, G.; Feng, H.; Husson, R.; Picot, N.; Provost, C.; et al. The new CNES-CLS18 global mean dynamic topography. *Ocean Sci.* **2021**, *17*, 789–808. [[CrossRef](#)]
43. Zingerle, P.; Pail, R.; Gruber, T.; Oikonomidou, X. The combined global gravity field model XGM2019e. *J. Geod.* **2020**, *94*, 66. [[CrossRef](#)]
44. Sandwell, D.T.; Harper, H.; Tozer, B.; Smith, W.H.F. Gravity field recovery from geodetic altimeter missions. *Adv. Space Res.* **2021**, *68*, 1059–1072. [[CrossRef](#)]
45. Guo, J.Y.; Liu, X.; Chen, Y.N.; Wang, J.B.; Li, C.M. Local normal height connection across sea with ship-borne gravimetry and GNSS techniques. *Mar. Geophys. Res.* **2014**, *35*, 141–148. [[CrossRef](#)]
46. Hwang, C.; Parsons, B. Gravity anomalies derived from seasat, geosat, ERS-I and TOPEX/POSEIDON altimetry and ship gravity: A case study over the Reykjanes ridge. *Geophys. J. Int.* **1995**, *122*, 551–568. [[CrossRef](#)]
47. Pavlis, N.K.; Holmes, S.A.; Kenyon, S.C.; Factor, J. The development and evaluation of the Earth Gravitational Model 2008 (EGM2008). *J. Geophys. Res. Solid Earth* **2013**, *118*, 2633. [[CrossRef](#)]
48. Bucha, B.; Janák, J. A MATLAB-based graphical user interface program for computing functionals of the geopotential up to ultra-high degrees and orders: Efficient computation at irregular surfaces. *Comput. Geosci.* **2014**, *66*, 219–227. [[CrossRef](#)]
49. Gaultier, L.; Ubelmann, C.; Fu, L.-L. *SWOT Simulator Documentation. Release 2.3.0. Pasadena*; Jet Propulsion Laboratory, National Aeronautics and Space Administration: Pasadena, CA, USA, 2017.
50. Gaultier, L.; Ubelmann, C.; Fu, L.-L. The challenge of using future SWOT data for oceanic field reconstruction. *J. Atmos. Ocean Technol.* **2016**, *33*, 119–126. [[CrossRef](#)]
51. Smith, G.N. *Mean Gravity Anomaly Prediction from Terrestrial Gravity Data and Satellite Altimeter Data*; Ohio State University: Columbus, OH, USA, 1974.
52. Rapp, R.H. *Gravity Anomaly Recovery from Satellite Altimetry Data Using Least Squares Collocation Techniques*; Ohio State University: Columbus, OH, USA, 1974.
53. Zhu, C.C.; Guo, J.Y.; Hwang, C. How HY2A/GM altimeter performs in marine gravity derivation: Assessment in the South China Sea. *Geophys. J. Int.* **2019**, *219*, 1056–1064. [[CrossRef](#)]
54. Hwang, C. Inverse vening meinesz formula and deflection-geoid formula: Applications to the predictions of gravity and geoid over the South China Sea. *J. Geod.* **1998**, *72*, 304–312. [[CrossRef](#)]
55. Zhu, C.; Guo, J.Y.; Gao, J.Y.; Liu, X.; Hwang, C.; Yu, S.W.; Yuan, J.J.; Ji, B.; Guan, B. Marine gravity determined from multi-satellite GM/ERM altimeter data over the South China Sea: SCSGA V1.0. *J. Geod.* **2020**, *94*, 50. [[CrossRef](#)]
56. Li, J.C.; Chen, J.Y.; Ning, J.S.; Chao, D.B. *Approximation Theory of the Earth Gravity Field and Determination of the Chinese Gravity Geoid Model 2000*; Wuhan University Press: Wuhan, China, 2003.
57. Wan, X.Y.; Annan, R.F.; Jin, S.G.; Gong, X.Q. Vertical deflections and gravity disturbances derived from HY-2A data. *Remote Sens.* **2020**, *12*, 2287. [[CrossRef](#)]
58. Barnoud, A.; Picard, B.; Meyssignac, B.; Marti, F.; Ablain, M.; Roca, R. Reducing the Uncertainty in the Satellite Altimetry Estimates of Global Mean Sea Level Trends Using Highly Stable Water Vapor Climate Data Records. *J. Geophys. Res.-Ocean.* **2023**, *128*, e2022JC019378. [[CrossRef](#)]

59. Rapp, R.H. Geos 3 data processing for the recovery of geoid undulations and gravity anomalies. *J. Geophys. Res. Atmos.* **1979**, *84*, 3784–3792. [[CrossRef](#)]
60. Hwang, C. *High Precision Gravity Anomaly and Sea Surface Height Estimation from Geo-3/Seasat Altimeter Data*; Ohio State University: Columbus, OH, USA, 1989.
61. Liang, W.; Li, J.C.; Xu, X.Y.; Zhang, S.J.; Zhao, Y.Q. A high-resolution earth's gravity field model SGG-UGM-2 from GOCE, GRACE, satellite altimetry, and EGM2008. *Engineering* **2020**, *6*, 860–878. [[CrossRef](#)]

Disclaimer/Publisher's Note: The statements, opinions and data contained in all publications are solely those of the individual author(s) and contributor(s) and not of MDPI and/or the editor(s). MDPI and/or the editor(s) disclaim responsibility for any injury to people or property resulting from any ideas, methods, instructions or products referred to in the content.